Chaotic synchronization between atomic clocks

Aniket Patra,[1] Boris L. Altshuler,[2] and Emil A. Yuzbashyan[1]

[1]*Department of Physics and Astronomy, Rutgers University, Piscataway, New Jersey 08854, USA*
[2]*Department of Physics, Columbia University, New York, New York 10027, USA*

We predict synchronization of the chaotic dynamics of two atomic ensembles coupled to a heavily damped optical cavity mode. The atoms are dissipated collectively through this mode and pumped incoherently to achieve a macroscopic population of the cavity photons. Even though the dynamics of each ensemble are chaotic, their motions repeat one another. In our system, chaos first emerges via quasiperiodicity and then synchronizes. We identify the signatures of synchronized chaos, chaos, and quasiperiodicity in the experimentally observable power spectra of the light emitted by the cavity.

I. INTRODUCTION

It is generally challenging to predict the long-term behavior of a chaotic system, e.g., weather, due to its sensitive dependence on initial conditions. However, there are special chaotic systems where the dynamics of one part are locked or *synchronized* with those of the other part or parts [1,2]. As a result, the asymptotic behavior of certain dynamical variables is fully predictable in spite of the overall chaotic nature. Different mechanisms of obtaining chaotic synchronization have been studied in, for example, electrical circuits [3,4], coupled lasers [5–7], oscillators in laboratory plasma [8], population dynamics [9], and earthquake models [10]. In this paper, we report chaotic synchronization in a novel physical system, namely, between two *mutually coupled* ensembles of atoms in a driven-dissipative experimental setup. This is unlike most other examples of chaotic synchronization, where the coupling between the two parts is unidirectional. In the chaotic synchronized phase, our system has potential applications in secure communication [1–5].

We consider two spatially separated ensembles of, e.g., ^{87}Rb atoms inside a bad (leaky) optical cavity, see Fig. 1. The atoms are collectively dissipated through a Rabi coupling to a heavily damped cavity mode and pumped with a transverse laser to achieve a macroscopic population of the cavity photons [11]. A single atomic ensemble coupled to a bad cavity has been proposed as a source of ultracoherent radiation for an atomic clock [12]. The two ensembles in our setup, therefore, represent two interacting atomic clocks [13]. Previous work obtained main nonequilibrium phases of this system [13,14], see the inset in Fig. 2.

In this paper, we study a finite region of the phase diagram—the orange (nonsynchronized chaos) and red (synchronized chaos) points in region III of Fig. 1—where the light radiated by the cavity behaves chaotically. Here chaos appears via quasiperiodicity [15–17]. Initially, chaotic trajectories fill up extended regions in the configuration space, see Fig. 3(e). We discover a subregion inside the chaotic phase where dynamics are confined to a flat hypersurface [Fig. 3(h)], called the synchronization manifold. Essentially, the time dependence of one ensemble follows that of the other. We also study signatures of these novel behaviors in the power spectra of the radiated light. Unlike the quasiperiodic power spectrum [Fig. 3(c)], which consists of discrete peaks, the chaotic one [Fig. 3(f)] is a continuum. The chaotic synchronized spectrum [Fig. 3(i)] additionally has a reflection symmetry about zero and no peak at zero frequency, see the insets in Figs. 3(f) and Fig. 3(i).

II. NONCHAOTIC PHASES

We model our system (cf. Fig. 2) with the following master equation for the density matrix ρ:

$$\dot{\rho} = -\iota[\hat{H}, \rho] + \kappa \mathcal{L}[a]\rho + W \sum_{\tau=A,B} \sum_{j=1}^{N} \mathcal{L}[\hat{\sigma}_{j+}^{\tau}]\rho, \quad \text{(1a)}$$

$$\hat{H} = \omega_0 \hat{a}^\dagger \hat{a} + \sum_{\tau=A,B} \left[\omega_\tau \hat{S}_\tau^z + \frac{\Omega}{2} \left(\hat{a}^\dagger \hat{S}_\tau^- + \hat{a} \hat{S}_\tau^+ \right) \right]. \quad \text{(1b)}$$

The Hamiltonian $\hat{H}$ describes two atomic ensembles, A and B, Rabi coupled (with frequency Ω) to the cavity mode ω_0, where $\hat{a}^\dagger (\hat{a})$ create (annihilate) cavity photons. Each ensemble contains a large number of atoms, e.g., $N \approx 10^6$ of ^{87}Rb atoms [11,13]. We focus on the lasing transition between two atomic levels. Consequently, we describe individual atoms with Pauli matrices and the atomic ensembles with collective spin operators $\hat{S}_z^{A,B} = \frac{1}{2} \sum_{j=1}^{N} \hat{\sigma}_{jz}^{A,B}$ and $\hat{S}_\pm^{A,B} = \sum_{j=1}^{N} \hat{\sigma}_{j\pm}^{(A,B)}$. Experimentally, the level-spacings ω_τ are controlled with two distinct Raman dressing lasers [11]. We model the energy-nonconserving processes [decay of the bad cavity mode with a rate $\kappa (\gg 1)$, and incoherent pumping by external lasers at an effective repump rate W] by Lindblad superoperators,

$$\mathcal{L}[\hat{O}]\rho \equiv \frac{1}{2}(2\hat{O}\rho\hat{O}^\dagger - \hat{O}^\dagger\hat{O}\rho - \rho\hat{O}^\dagger\hat{O}). \quad \text{(2)}$$

Using the adiabatic approximation [18], which is exact in the limit $\kappa \to \infty$, we eliminate the cavity mode replacing $\hat{a} \to \frac{\iota\Omega}{\kappa} \sum_\tau \hat{S}_\tau^-$. Finally, in the rotating frame, where frequencies are shifted by the mean level-spacing (it is equal to the clock transition frequency, which is ≈ 6.8 GHz for ^{87}Rb), we
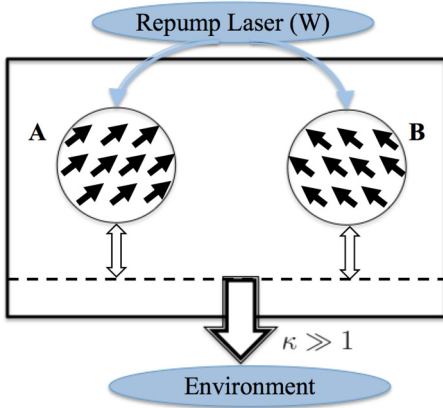
FIG. 1. Cartoon depicting the driven-dissipative experimental setup with two atomic ensembles inside a bad cavity. In ensembles A and B, the solid arrows denote individual atoms. The thick double-headed arrows correspond to the Rabi coupling between the ensembles and the cavity mode (dashed line). The rate of loss of photons from the cavity is κ.

derive semiclassical evolution equations using the mean-field approximation, $\langle \hat{O}_1 \hat{O}_2 \rangle \approx \langle \hat{O}_1 \rangle \langle \hat{O}_2 \rangle$,

$$\dot{s}_\pm^\tau = \left(\pm \iota \omega_\tau - \frac{W}{2} \right) s_\pm^\tau + \frac{1}{2} s_z^\tau l_\pm, \tag{3a}$$

$$\dot{s}_z^\tau = W \left(1 - s_z^\tau \right) - \frac{1}{4} s_+^\tau l_- - \frac{1}{4} s_-^\tau l_+, \tag{3b}$$

where $\tau = A, B$, $s_\pm^\tau = \frac{2}{N}(\langle \hat{S}_x^\tau \rangle \pm i \langle \hat{S}_y^\tau \rangle)$, $s_z^\tau = \frac{2}{N} \langle \hat{S}_z^\tau \rangle$, $\boldsymbol{l} = \frac{2}{N}(\langle \hat{\boldsymbol{S}}^A \rangle + \langle \hat{\boldsymbol{S}}^B \rangle)$ is the total classical spin, $\omega_A = \delta/2$, and $\omega_B = -\delta/2$. In Eq. (3) and from now on, we express the detuning δ and the repump rate W in the units of the collective decay rate $N\Gamma_c \equiv \frac{N\Omega^2}{\kappa}$ (≈ 1.4 kHz for a typical experimental setup [11]) and replace $(N\Gamma_c)t \rightarrow t$.

The mean-field equations of motion possess two symmetries: (1) Axial symmetry $\boldsymbol{s}^\tau \rightarrow \mathbb{R}(\phi) \cdot \boldsymbol{s}^\tau$, where $\mathbb{R}(\phi)$ is a rotation by an angle ϕ around the z axis. Indeed, the replacement $s_\pm^\tau \rightarrow s_\pm^\tau e^{\pm \iota \phi}$ leaves Eq. (3) unchanged. (2) $\mathbb{Z}_2$ symmetry $\boldsymbol{s}^\tau \rightarrow \Sigma \circ \mathbb{R}(\phi_0) \cdot \boldsymbol{s}^\tau$ which involves a rotation around the z axis by a fixed angle ϕ_0 followed by an interchange,

$$\Sigma : \left(s_\pm^A, s_z^A, s_\pm^B, s_z^B \right) \longrightarrow \left(s_\mp^B, s_z^B, s_\mp^A, s_z^A \right), \tag{4}$$

of ensembles A and B while flipping the sign of s_y. The $\mathbb{Z}_2$ symmetric solutions obey $\boldsymbol{s}^\tau = \Sigma \circ \mathbb{R}(\phi_0) \cdot \boldsymbol{s}^\tau$, where the value of ϕ_0 depends on the initial condition. This constraint defines a 4D $\mathbb{Z}_2$-symmetric submanifold. All attractors in Fig. 1, except the normal phase, spontaneously break the axial symmetry. This implies that for each (δ, W) point there is a family of attractors related by a rotation $\mathbb{R}(\phi)$ around the z axis, where ϕ depends on the initial condition.

The limit cycle (periodically modulated superradiance) in the green region of Fig. 1 possesses $\mathbb{Z}_2$ symmetry, which breaks spontaneously across the black dashed line. In the absence of any symmetry, the interaction between the two spins introduces additional frequencies. The ratio of two such frequencies being irrational causes quasiperiodicity, which eventually gives way to chaos. At its inception, the chaotic attractor is completely asymmetric. As we decrease δ while
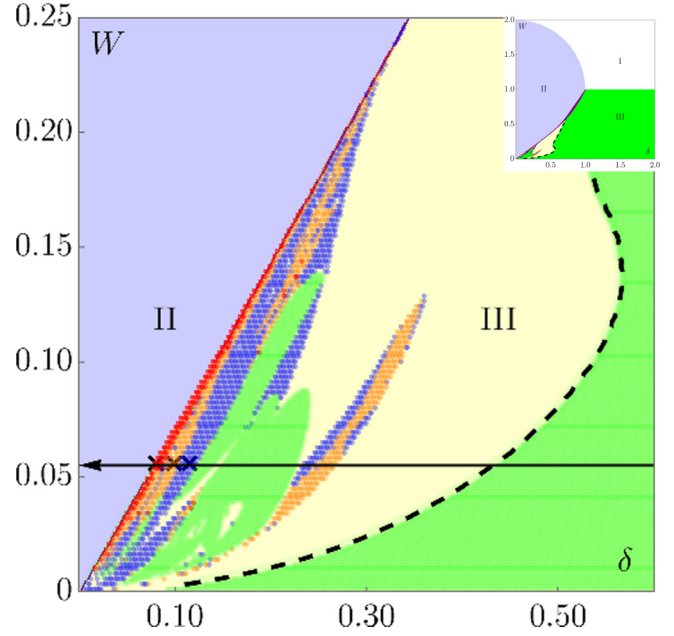

FIG. 2. Nonequilibrium phase diagram for two atomic ensembles in a bad optical cavity. W is the repump rate and and δ is the detuning between the atomic level spacings of the two ensembles in the units of the collective decay rate $N\Gamma_c$. The inset shows the full phase diagram with phases I (normal, non-superradiant phase), II (monochromatic superradiance), and III (amplitude-modulated superradiance). The main picture is a blowup of the region near the origin. Green points correspond to $\mathbb{Z}_2$-symmetric (with respect to the interchange of the two ensembles) collective oscillations (limit cycle). The $\mathbb{Z}_2$ symmetry breaks spontaneously across the black dashed line. In the yellow region to the left of this line, the attractor is a symmetry-broken limit cycle. Dark blue, orange, and red points indicate quasiperiodicity, chaos, and synchronized chaos, respectively.

keeping W fixed, one spin gets locked to the other. We interpret this synchronized chaotic phase as spontaneous restoration of the $\mathbb{Z}_2$ symmetry. In this phase, the conditional Lyapunov exponent becomes negative, while the maximum Lyapunov exponent remains positive [1,2] as shown in Fig. 4. As we cross over to region II, chaos disappears altogether. One is left with monochromatic superradiance, which is a fixed point of Eq. (3) [14]. Separately, we also note that dynamics of a single atomic ensemble coupled to a bad cavity show no chaos or quasiperiodicity. In fact, this case corresponds to $\delta = 0$ in Eq. (3), i.e., to the vertical axis of the phase diagram in Fig. 1, where only phases I and II are present [14].

III. SYNCHRONIZATION OF CHAOS

In the rest of this paper, we analyze the evolution from quasiperiodicity to synchronized chaos with the help of Poincaré sections, Lyapunov exponents, and power spectra. We define the maximum Lyapunov exponent $\lambda(t)$ as usual,

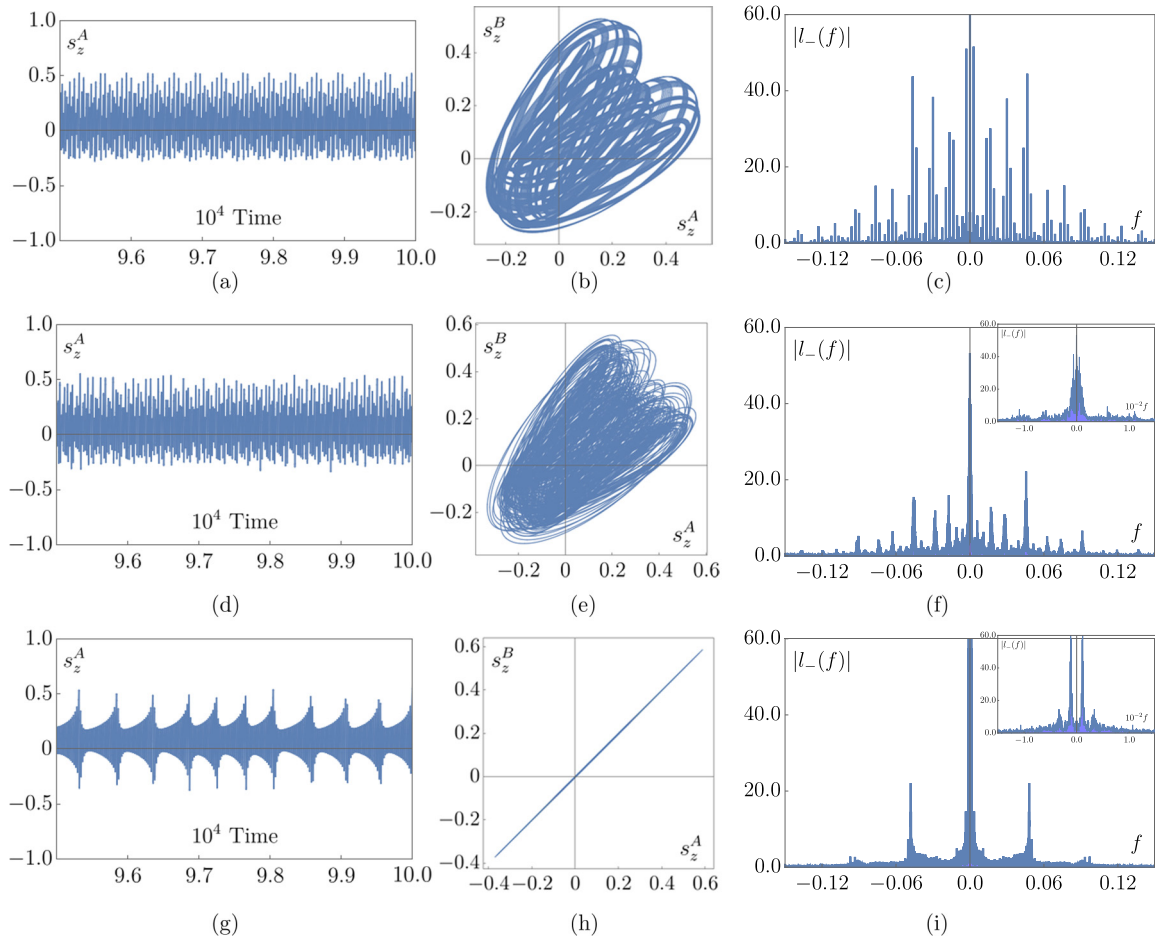$$\lambda(t) = \lim_{d(0) \to 0} \frac{1}{t} \ln \left[\frac{d(t)}{d(0)} \right], \tag{5}$$

FIG. 3. Three types of dynamics of two coupled atomic clocks, i.e., of two atomic ensembles coupled to a strongly damped cavity mode. The classical spins s^τ representing the two clocks ($\tau = A$ and B) obey mean-field equations of motion (3). The three rows of plots from top to bottom represent quasiperiodic ($\delta = 0.115$, $W = 0.055$), chaotic ($\delta = 0.1$, $W = 0.055$), and synchronized chaotic ($\delta = 0.080$, $W = 0.055$) attractors, respectively. We marked these three (δ, W) pairs with crosses on the solid black horizontal arrow in Fig. 1. The three columns of plots from left to right show s_z^A vs time [Figs. 3(a), 3(d), and 3(g)], s_z^A vs s_z^B [Figs. 3(b), 3(e), and 3(h)], and the power spectra of radiated light [Figs. 3(c), 3(f), and 3(i)], respectively. In the quasiperiodic spectrum (c), the main peaks are at integer multiples of $f_1 \approx 1.6 \times 10^{-2}$, whereas the distance between auxiliary peaks is $f_2 \approx 3.0 \times 10^{-3}$. In the insets to plots (f) and (i) we magnified the region near $f = 0$ to show the presence or absence of the peak at the origin.

where $d(t)$ is the distance in the 6D real space of six components of vectors s^A and s^B. The conditional Lyapunov exponent is the maximum Lyapunov exponent for directions transverse to the synchronization manifold, see Eq. (7). For both chaotic and synchronized chaotic attractors $\lambda(t)$ converges to a positive value ($\approx 10^{-2} \pm 10^{-5}$), whereas for the quasiperiodic attractor it vanishes ($\pm 10^{-5}$), see the inset in Fig. 4.

A Poincaré section of an attractor is the set of points where its trajectory crosses a plane cutting the attractor into two, counting only the crossings that occur in one direction [15,19]. To obtain a 2D representation, we show the Poincaré sections for the A spin only in Fig. 5. Those for the B spin are qualitatively similar. We cut the trajectory of the A spin with the plane $s_z^A = \text{const} = \frac{1}{t_1} \int_{t_0}^{t_0+t_1} s_z^A dt$ parallel to the $s_x^A - s_y^A$ plane, where t_0 and t_1 are sufficiently large.

Poincaré sections of quasiperiodic trajectories appear as continuous curves. Consider, e.g., a two-frequency quasiperiodic motion. It occurs on a 2D torus in the 6D space of

six components of both classical spins. We expect the full Poincaré section to be a closed non-self-intersecting 5D curve. However, when looking only at the A spin, we project this curve onto a 2D plane. The resulting Poincaré section is still a continuous curve, but it can now intersect itself as in the leftmost plot in Fig. 5. The Poincaré section of a chaotic trajectory appears as a smudge of random points. Finally, the section of a chaotic synchronized trajectory is a collection of disjoint segments highlighting both the chaotic and constricted (to the synchronization manifold) nature of the dynamics.

An experimentally observable quantity is the power spectrum, $|\boldsymbol{E}(f)|^2$, of the light emitted by the cavity [14,20]. Here $\boldsymbol{E}(f)$ is the Fourier transform of the (complex) radiated electric field and f is the frequency. Within the mean-field approximation, we find $|\boldsymbol{E}(f)|^2 \propto |l_-(f)|^2$, where $l_- = l_x - \iota l_y$ and $\boldsymbol{l}$ is the total classical spin. The quasiperiodic spectrum [Fig. 3(c)] has main peaks at $0, \pm f_1, \pm 2f_1, \ldots$, with auxiliary peaks spaced at f_2 bunched around them.
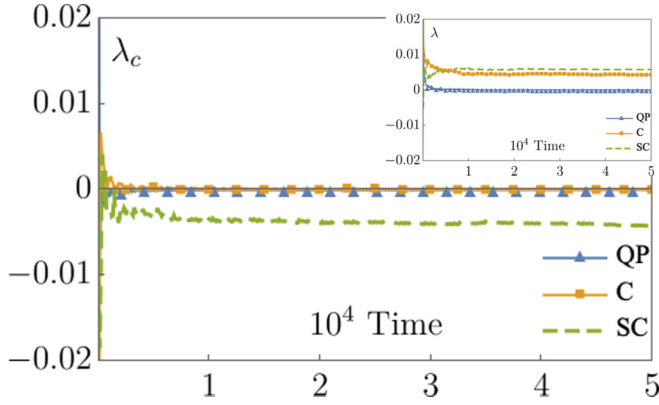
FIG. 4. Conditional Lyapunov exponents $\lambda_c(t)$ quickly saturate to zero for quasiperiodic (blue triangles) and chaotic (yellow squares) attractors. The values of the detuning δ and the repump rate W are the same as in Fig. 3. For synchronized chaos (green dashed line) λ_c is negative. The inset shows the maximum Lyapunov exponent $\lambda(t)$. As expected, for chaos and synchronized chaos λ is positive, whereas for quasiperiodicity it saturates to zero.

We did not observe more than two-frequency quasiperiodicity. While it is generally difficult to differentiate between chaotic and quasiperiodic spectra [21], in our system the latter are visibly discrete. Nevertheless, we do not rely on this feature and use maximum Lyapunov exponents to distinguish quasiperiodicity and chaos in Fig. 1. Note that although the chaotic spectrum is continuous, it features distinct peaks that are independent of the initial conditions [Fig. 3(f)]. In contrast to the spectrum of the synchronized chaotic attractor in Fig. 3(i), both chaotic and quasiperiodic power spectra have prominent peaks at the origin and no reflection symmetry.

Near the boundary between phases II and III in Fig. 1 (red points), we observe synchronized chaos. Since the dynamics in this subregion restore the $\mathbb{Z}_2$ symmetry, the solutions are confined to the 4D $\mathbb{Z}_2$-symmetric submanifold. We write the two constraint relations (independent of initial condition)

as

$$\left(s_x^A\right)^2 + \left(s_y^A\right)^2 = \left(s_x^B\right)^2 + \left(s_y^B\right)^2, \quad s_z^A = s_z^B. \qquad (6)$$

For our purposes, these relations define the synchronization manifold. Coordinates spanning the "transverse manifold" (complementary to the synchronization manifold) are

$$\mathsf{n}_1 \equiv \left(s_x^A\right)^2 + \left(s_y^A\right)^2 - \left(s_x^B\right)^2 - \left(s_y^B\right)^2,$$
$$\mathsf{n}_2 \equiv s_z^A - s_z^B. \qquad (7)$$

We derive the evolution equations for the transverse subsystem from Eq. (3) as

$$\dot{\mathsf{n}}_1 = \frac{1}{2}\left(l_z - 2W\right)\mathsf{n}_1 + \frac{1}{2}\left(l_x^2 + l_y^2\right)\mathsf{n}_2, \qquad (8a)$$

$$\dot{\mathsf{n}}_2 = -\frac{\mathsf{n}_1}{2} - W\mathsf{n}_2. \qquad (8b)$$

To compute the conditional Lyapunov exponent for an attractor, we first determine its l_z and $l_x^2 + l_y^2$ with the help of Eq. (3). These serve as time-dependent coefficients in Eqs. (8). In principle, we should linearize Eqs. (8) in small deviations $\Delta\mathsf{n}_1$ and $\Delta\mathsf{n}_2$. However, since these equations are already linear, we simply redefine n_1 and n_2 to be such arbitrary infinitesimal deviations in transverse directions and numerically simulate Eqs. (8). The conditional Lyapunov exponent is the rate of growth of distances in the transverse manifold, i.e., it is given by Eq. (5), where $d = \sqrt{\mathsf{n}_1^2 + \mathsf{n}_2^2}$ is the transverse distance. For chaotic synchronized trajectories $\lambda_c \approx -10^{-2} \pm 10^{-5}$ for $t \geqslant 5 \times 10^4$, whereas for chaotic ones $\lambda_c \approx \pm 10^{-5}$ (Fig. 4). On the other hand, maximum Lyapunov exponents λ for both chaos and synchronized chaos behave similarly.

In the Appendix, we explain the emergence of the synchronized chaos in our system via *tangent bifurcation intermittency* of the $\mathbb{Z}_2$-symmetric limit cycle. As a result, synchronized chaotic trajectories spend most of their time in the vicinity of the now unstable $\mathbb{Z}_2$-symmetric limit cycle, see Fig. 6 a. Further, we observe in Fig. 7 that the synchronized chaotic
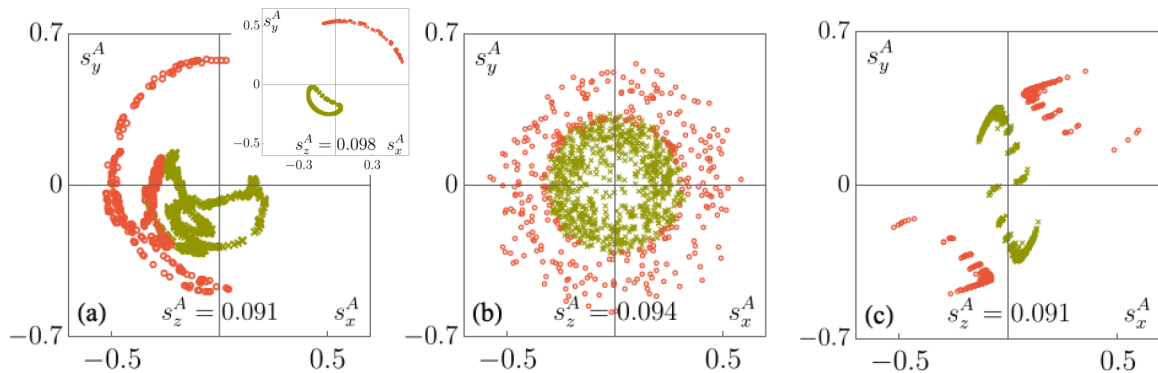

FIG. 5. Poincaré sections of the spin s^A trajectory for (a) quasiperiodic ($\delta = 0.115$, $W = 0.055$), (b) chaotic ($\delta = 0.1$, $W = 0.055$), and (c) synchronized chaotic ($\delta = 0.080$, $W = 0.055$) attractors. These values of δ and W are the same as in Figs. 3 and 4. We section the trajectories with a plane $s_z^A = \text{const}$ as explained in the main text. Orbits cross the plane either from below (red circles) or from above (green crosses) generating two distinct Poincaré sections. The inset in (a) shows an example ($\delta = 0.24$, $W = 0.055$) of non-self-intersecting Poincaré sections of a quasiperiodic attractor. The difference between Poincaré sections of chaotic and synchronized chaotic trajectories of spin s^A is due to the restriction of the dynamics to the synchronization manifold in the latter case.
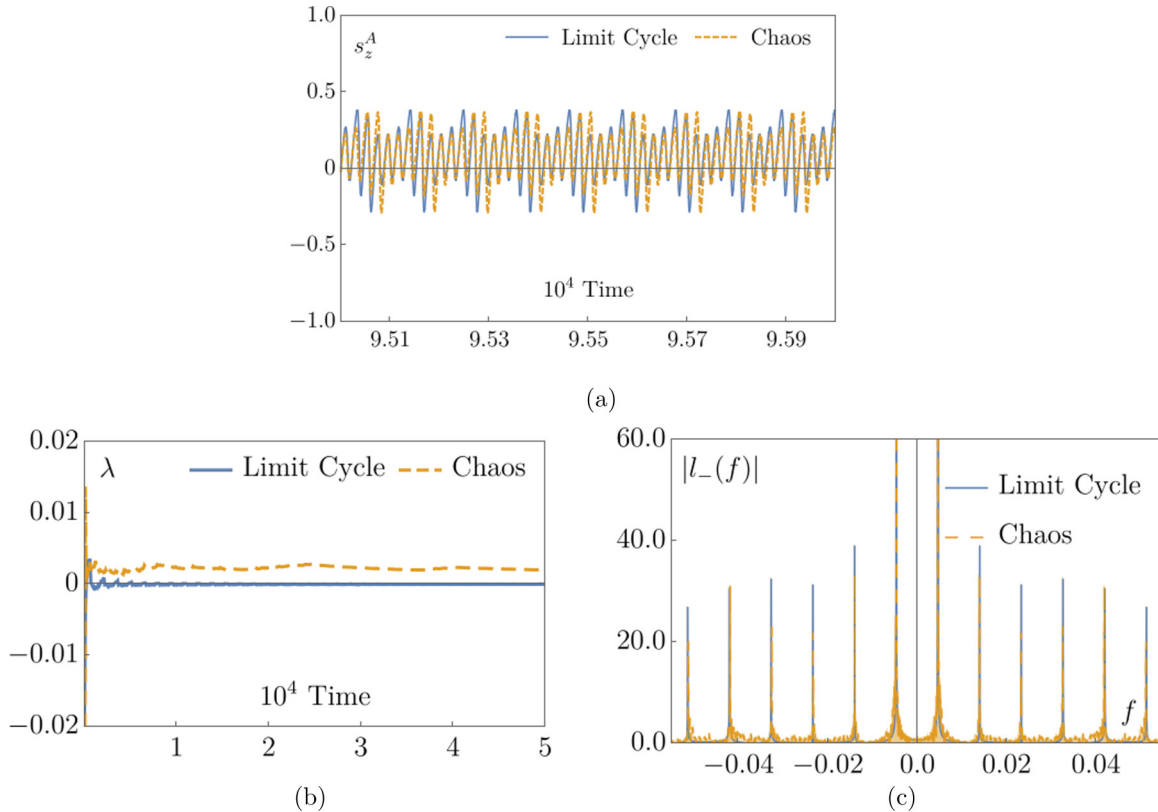
FIG. 6. Comparison of $\mathbb{Z}_2$-symmetric limit cycle ($\delta = 0.107$, $W = 0.055$) with synchronized chaos ($\delta = 0.106$, $W = 0.055$). For $W = 0.055$, the $\mathbb{Z}_2$-symmetric limit cycle loses stability in the $\mathbb{Z}_2$-symmetric submanifold via tangent bifurcation intermittency between $\delta = 0.107$ and 0.106. However, note that non-$\mathbb{Z}_2$-symmetric initial conditions produce quasiperiodicity for both sets of (δ, W). (a) $s_z^A(t)$ for the same initial condition. The synchronized chaotic trajectory closely follows the periodic trajectory. (b) Lyapunov exponents λ reveal the chaotic nature ($\lambda > 0$) of the dashed yellow trajectory. (c) The power spectra. For the $\mathbb{Z}_2$-symmetric limit cycle the peaks are at $\pm f_0$, $\pm 3 f_0$, $\pm 5 f_0$, ..., where $f_0 \approx 0.0047$. In the chaotic spectrum, the prominent peaks are at the same positions as for the limit cycle. Nevertheless, all frequencies acquire nonzero weights at the advent of chaos in the $\mathbb{Z}_2$-symmetric submanifold.

attractor starts off being unstable in the full phase space. Only close to the boundary of phases II and III (red points) this attractor becomes sufficiently attractive [22]. The restoration of the $\mathbb{Z}_2$ symmetry explains the reflection symmetric (with no peak at zero) power spectrum of the synchronized chaotic attractor, see Figs. 3(i).

In the master equation (1) we neglected the effects of spontaneous emission and inhomogeneous life time T_2. Since the chaotic synchronization is an asymptotic solution of mean-field equations (3), one needs to clarify the effects of these neglected decay processes at large times. To this effect, we show in Fig. 8 that the system reaches its steady state for $\delta = 0.080$ and $W = 0.055$ [same as in Figs. 3(g), 3(h), and 3(i)] in approximately 0.14 s ($\approx$200 time steps). In a typical experimental setup the timescale related to spontaneous emission can be pushed to 100 s, whereas T_2 can be as large as 1 s [23]. This comparison of the experimental timescales with the timescale relevant for the observation of chaotic synchronization validates the master equation (1).

Another impediment for the observation of chaotic synchronization is the limited efficiency of the atomic traps that are required to localize the atomic ensembles. Current experiments [24] are able to observe superradiant emission for as long as 120 ms. This should be enough to detect the signature of chaotic synchronization: exponential attenuation

of $s_z^A - s_z^B$. For example, in Fig. 8 this is seen between 70 and 140 ms. Loss of atoms from the traps with different rates can also lead to atom number imbalance between the ensembles, which in turn breaks the $\mathbb{Z}_2$ symmetry. This effect, however, affects the steady states only perturbatively, see Fig. 9.

IV. CONCLUSION

In conclusion, we have predicted chaotic synchronization of the dynamics of two atomic ensembles collectively coupled to a heavily damped cavity mode. Synchronized chaos emerges from quasiperiodicity by way of (asymmetric) chaos. Its origin is in the tangent bifurcation intermittency of the $\mathbb{Z}_2$-symmetric limit cycle (see Appendix). We distinguish the three phases theoretically, by analyzing the Poincaré sections and maximum and conditional Lyapunov exponents. Open questions include the effects of coupling to multiple cavity modes and of quantum fluctuations. A quantum analog to our system, where the overall system is chaotic, but a subsector is not, is known [25]. It would also be interesting to explore prospects of realizing a viable steganography [1–5] (instead of hiding the meaning of transmitted message, hide the existence of the message itself) protocol with our system. In particular, it is not apparent how to send a message over a long distance.
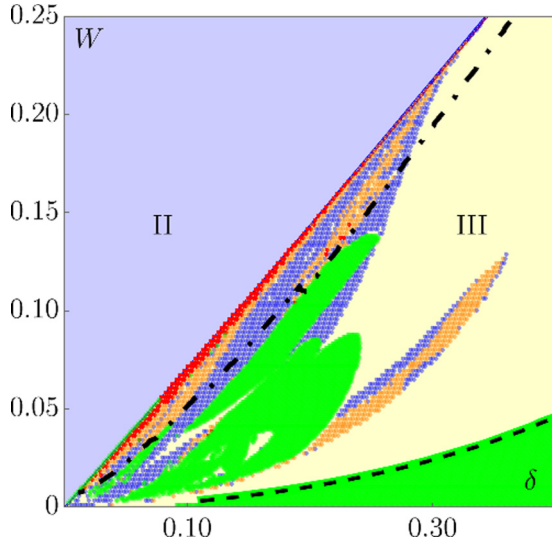
FIG. 7. Onset of chaos via tangent bifurcation intermittency in the dynamics confined to the $\mathbb{Z}_2$-symmetric submanifold. Initial conditions lying in this submanifold lead to (synchronized) chaos to the left of the dot-dashed line. We superimposed this line onto Fig. 1. Notice that at its birth the synchronized chaotic attractor is unstable, since only the red points in the immediate vicinity of the II–III boundary produce synchronized chaos for generic initial conditions in the full phase space.

APPENDIX: TANGENT BIFURCATION INTERMITTENCY IN THE $\mathbb{Z}_2$-SYMMETRIC SUBMANIFOLD

Recall that the synchronized chaotic attractor spontaneously restores the $\mathbb{Z}_2$ symmetry between the two ensembles of atoms. Therefore, to gain further insight into it, we investigate $\mathbb{Z}_2$-symmetric dynamics in this section.

After a rotation around the z axis by an angle ϕ_0, which depends on the initial condition, $\mathbb{Z}_2$-symmetric dynamics are invariant with respect to the replacement (4), i.e.,

$$s_x^B = s_x^A, \quad s_y^B = -s_y^A, \quad s_z^B = s_z^A. \tag{A1}$$

This implies $l_x = 2s_x^A = 2s_x^B$, $l_y = 0$ and the mean-field equations of motion (3) for the spin $\boldsymbol{s}^A$ become

$$\dot{s}_x = -\frac{\delta}{2}s_y - \frac{W}{2}s_x + s_z s_x, \tag{A2a}$$

$$\dot{s}_y = \frac{\delta}{2}s_x - \frac{W}{2}s_y, \tag{A2b}$$

$$\dot{s}_z = W(1 - s_z) - s_x^2, \tag{A2c}$$

where we dropped the superscript A for simplicity. The spin $\boldsymbol{s}^B$ is related to $\boldsymbol{s}^A$ by Eq. (A1).

Note that Eq. (A2) is very different from the mean-field equations of motion for a single atomic ensemble coupled to a bad cavity. We obtain the latter from the two-ensemble equations (3) by setting one of the spins, say $\boldsymbol{s}^B$, to zero. Then, by going into a frame uniformly rotating with frequency
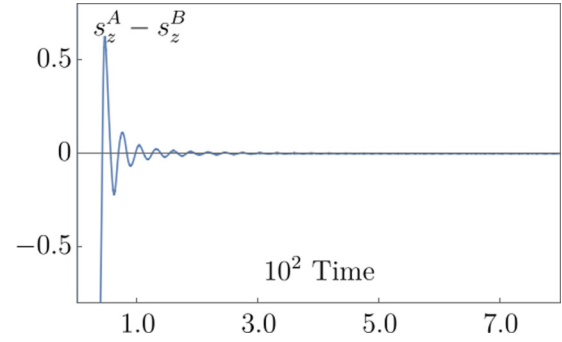

FIG. 8. Onset of synchronized chaos. The plot of $s_z^A - s_z^B$ vs time, for $\delta = 0.080$ and $W = 0.055$ shows that the synchronization of chaos is attained in approximately $200(N\Gamma_c)^{-1} \approx 0.14$ s.

$\omega_A = \delta/2$, we eliminate δ from the one-ensemble equations of motion. Thus, single ensemble (one spin) equations correspond to setting $\delta = 0$ in Eq. (3). Indeed, summing Eq. (3) for $\delta = 0$ over τ and rescaling $\boldsymbol{l} \to 2\boldsymbol{l}$, $W \to 2W$, and $2t \to t$ we obtain the one-ensemble equations of motion in the rotating frame. This implies that the nonequilibrium phase diagram for a single ensemble is just the vertical, $\delta = 0$ axis of the two-ensemble phase diagram in Fig. 1 with the rescaling $2W \to W$. It consists of two fixed points (normal phase and monochromatic superradiance), see Ref. [14] for details. In contrast, Eq. (A2) depends on two dimensionless parameters δ and W in an essential way and, consequently, has much richer dynamics as we now discuss.

While solutions of Eq. (A2) are consistent with the full mean-field equations (3), their stability in the full phase space is not guaranteed. The three types of solutions of Eq. (A2) are fixed points, periodic ($\mathbb{Z}_2$ symmetric limit cycle), and chaotic (synchronized chaos). In the parentheses we mention the equivalent solutions of Eq. (3).

Consider the portion of the phase diagram to the left of the $\mathbb{Z}_2$-symmetry-breaking line (black dashed line) in Fig. 6. Although the $\mathbb{Z}_2$-symmetric limit cycle loses stability in the
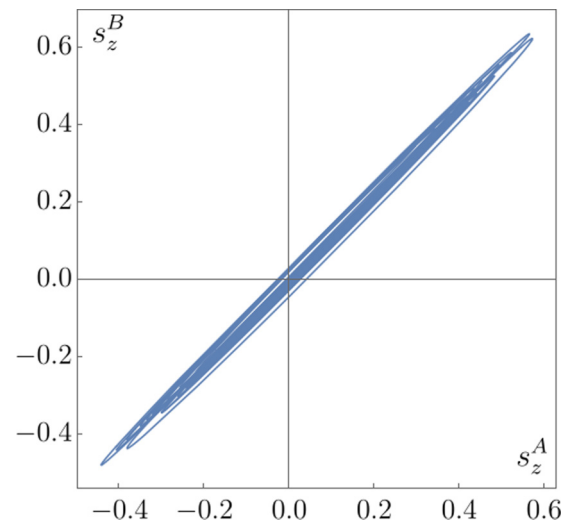

FIG. 9. Perturbative effect on synchronized chaos of imbalanced atom number between the two ensembles. We plot asymptotic s_z^B vs s_z^A for the same δ and W as in Fig. 3(h), but $N^A/N_{av} = 0.95$ as opposed to $N^A/N_{av} = 1$ in Fig. 3(h). Here $N_{av} = (N^A + N^A)/2$.

full phase space, it is still stable on the $\mathbb{Z}_2$-symmetric submanifold. As we move toward the phase II–III boundary, the periodic solution eventually loses stability on the dot-dashed line in Fig. 6 even on the $\mathbb{Z}_2$-symmetric submanifold, giving rise to chaos. We determine this line by computing the maximum Lyapunov exponent λ with the help of Eqs. (A3) and (A2). To the left of the dot-dashed line $\lambda > 0$, see, e.g., Fig. 7(b). Additionally, we prove the loss of stability employing a Floquet analysis of Eq. (A2).

The abrupt transition, and the proximity of the periodic and chaotic attractors suggest *tangent bifurcation intermittency* [15]. To illustrate this closeness we compare a chaotic spectrum with an adjacent periodic one in Fig. 7(c). Below, we provide the final proof in support of this claim by studying the evolution of the Floquet multipliers.

Floquet analysis. Our goal is to analyze the stability of the periodic solutions of the reduced equations (A2). To that end, we first summarize the Floquet analysis. Write the solution of Eq. (A2) as $s + \Delta s$, where s is the periodic solution with period T, and Δs is a perturbation. Linearizing Eq. (A2) with respect to the perturbation, we obtain a set of linear equations with time-dependent coefficients

$$\frac{d\Delta s_x}{dt} = \left(s_z - \frac{W}{2}\right)\Delta s_x - \frac{\delta}{2}\Delta s_y + s_x\Delta s_z, \quad \text{(A3a)}$$

$$\frac{d\Delta s_y}{dt} = \frac{\delta}{2}\Delta s_x - \frac{W}{2}\Delta s_y, \quad \text{(A3b)}$$

$$\frac{d\Delta s_y}{dt} = -2s_x\Delta s_x - W\Delta s_z. \quad \text{(A3c)}$$

The next step is to determine the monodromy matrix $\mathbb{M} = [\mathbb{S}(0)]^{-1}\mathbb{S}(T)$ for Eq. (A3). Here $\mathbb{S}(t)$ is a 3×3 matrix. Its columns are any three linearly independent solutions of Eq. (A3), which we obtain numerically. The eigenvalues

of the monodromy matrix $\rho_i \equiv e^{\varkappa_i T}$ are known as Floquet multipliers and $\varkappa_i$ are the corresponding Floquet exponents. By Floquet's theorem, the general solution of Eq. (A3) is

$$\Delta s(t) = \sum_{i=1}^{3} C_i e^{\varkappa_i t} p_i(t), \quad \rho_i \equiv e^{\varkappa_i T}, \quad \text{(A4)}$$

where C_i are constants and $p_i(t)$ are linearly independent and periodic with period T vectors. The limit cycle loses stability when the absolute value of one of the Floquet multipliers becomes greater than one.

Further, notice that $\Delta s = \dot{s}$ is a purely periodic with period T solution of Eq. (A3). This implies that one of the Floquet multipliers is identically equal to one, so that Eq. (A4) takes the form

$$\Delta s(t) = C_1\dot{s}(t) + C_2 e^{\varkappa_2 t} p_2(t) + C_3 e^{\varkappa_3 t} p_3(t). \quad \text{(A5)}$$

Near the dot-dashed line in Fig. 6, the remaining Floquet multipliers ρ_2 and ρ_3 are both real. As we approach this line from the right, $|\rho_2|$ tends to one from below, while $|\rho_3|$ remains less than one across criticality.

This behavior of the Floquet multipliers implies (by definition) a tangent bifurcation intermittency route to chaos [15]. A key feature of this route to chaos is that the chaotic attractor right after the bifurcation remains close to the now unstable limit cycle for most of the time, which we indeed observe in Figs. 7(a) and 7(c). Further, the power spectrum of the $\mathbb{Z}_2$-symmetric limit cycle is known to have reflection symmetry and no peak at zero frequency [14]. The power spectrum of the synchronized chaotic attractor in Fig. 7(c) reproduces these features due to the proximity of its trajectory to the limit cycle.

[1] A. Uchida, *Optical Communication with Chaotic Lasers* (Wiley, New York, 2012).

[2] L. M. Pecora, T. L. Carroll, G. A. Johnson, and D. G. Mar, Fundamentals of Synchronization in Chaotic Systems, Concepts and Applications, Chaos **7**, 520 (1997).

[3] L. M. Pecora and T. L. Carroll, Synchronization in Chaotic Systems, Phys. Rev. Lett. **64**, 821 (1990).

[4] S. Hayes, C. Grebogi, E. Ott, and A. Mark, Experimental Control of Chaos for Communication, Phys. Rev. Lett. **73**, 1781 (1994).

[5] P. M. Alsing, A. Gavrielides, V. Kovanis, R. Roy and K. S. Thornburg, Jr., Encoding and decoding messages with chaotic lasers, Phys. Rev. E **56**, 6302 (1997).

[6] H. G. Winful and L. Rahman, Synchronized Chaos and Spatiotemporal Chaos in Array of Coupled Lasers, Phys. Rev. Lett. **65**, 1575 (1990).

[7] R. Roy and K. S. Thornburg, Jr., Experimental Synchronization of Chaotic Lasers, Phys. Rev. Lett. **72**, 2009 (1994).

[8] T. Fukuyama, R. Kozakov, H. Testrich, and C. Wilke, Spatiotemporal Synchronization of Coupled Oscillators in a Laboratory Plasma, Phys. Rev. Lett. **96**, 024101 (2006).

[9] B. Blasius, A. Huppert, and L. Stone, Complex dynamics and phase synchronization in spatially extended ecological systems, Nature **399**, 354 (1999).

[10] M. de Sousa Vieira, Chaos and Synchronized Chaos in an Earthquake Model, Phys. Rev. Lett. **82**, 201 (1999).

[11] J. M. Weiner, K. C. Cox, J. G. Bohnet, and J. K. Thompson, Phase synchronization inside a superradiant laser, Phys. Rev. A **95**, 033808 (2017).

[12] M. Xu and M. J. Holland, Conditional Ramsey Spectroscopy with Synchronized Atoms, Phys. Rev. Lett. **114**, 103601 (2015).

[13] M. Xu, D. A. Tieri, E. C. Fine, James K. Thompson, and M. J. Holland, Synchronization of Two Ensembles of Atoms, Phys. Rev. Lett. **113**, 154101 (2014).

[14] A. Patra, B. L. Altshuler, and E. A. Yuzbashyan, Driven-dissipative dynamics of atomic ensembles in a resonant cavity: Nonequilibrium phase diagram and periodically modulated superradiance, Phys. Rev. A **99**, 033802 (2019).

[15] R. C. Hilborn, *Chaos and Nonlinear Dynamics, An Introduction for Scientists and Engineers*, 2d ed. (Oxford University, Oxford, 2001).

[16] D. Ruelle and F. Takens, On the Nature of Turbulence, Commun. Math. Phys. **20**, 167 (1971).

[17] S. E. Newhouse, D. Ruelle, and F. Takens, Occurrence of Strange Axiom A Attractors near Quasi-periodic Flows on T^m, $m \geqslant 3$, Commun. Math. Phys. **64**, 35 (1978).

[18] R. Bonifacio, P. Schwendimann, and F. Haake, Quantum statistical theory of superradiance. I, Phys. Rev. A **4**, 302 (1971).

[19] W. Tucker, Computing accurate poincaré maps, Physica D **171**, 127 (2002).

[20] H. J. Carmichael, *An Open System Approach to Quantum Optics* (Springer-Verlag, Berlin, 1993).

[21] R. S. Dumont and P. Brumer, Characteristics of power spectra for regular and chaotic systems, J. Chem. Phys. **88**, 1481 (1988).

[22] K. Josić, Invariant Manifolds and Synchronization of Coupled Dynamical Systems, Phys. Rev. Lett. **80**, 3053 (1998).

[23] D. Meiser, J. Ye, D. R. Carlson, and M. J. Holland, Prospects for a Milihertz- Linewidth Laser, Phys. Rev. Lett. **102**, 163601 (2009).

[24] J. G. Bohnet, Z. Chen, J. M. Weiner, D. Meiser, M. J. Holland, and J. K. Thompson, A steady-state superradiant laser with less than one intracavity photon, Nature **484**, 78 (2012).

[25] V. A. Yurovsky, Long-lived states with well-defined spins in spin $-1/2$ homogeneous Bose gases, Phys. Rev. A **93**, 023613 (2016).